Nuclear cluster structure effect in ^{16}O+^{16}O collisions at the top RHIC energy

Xin-Li Zhao,[1,2,3] Guo-Liang Ma,[2,3,*] You Zhou,[4,†] Zi-Wei Lin,[5] and Chao Zhang[6]

[1] *College of Science, University of Shanghai for Science and Technology, Shanghai* 200093, *China*
[2] *Key Laboratory of Nuclear Physics and Ion-beam Application (MOE), Institute of Modern Physics, Fudan University, Shanghai 200433, China*
[3] *Shanghai Research Center for Theoretical Nuclear Physics, NSFC and Fudan University, Shanghai* 200438, *China*
[4] *Niels Bohr Institute, Jagtvej 155A, 2200 Copenhagen, Denmark*
[5] *Department of Physics, East Carolina University, Greenville, NC 27858, USA*
[6] *School of Science, Wuhan University of Technology, Wuhan, 430070, China*

The impact of nuclear structure has garnered considerable attention in the high-energy nuclear physics community in recent years. This work focuses on studying the potential nuclear cluster structure in ^{16}O nuclei using anisotropic flow observables in O + O collisions at 200 GeV. Employing an improved AMPT model with various cluster structure configurations, we find that an extended effective parton formation time is necessary to align with the recent STAR experimental data. In addition, we reveal that the presented flow observables serve as sensitive probes for differentiating configurations of α-clustering of ^{16}O nuclei. The systematic AMPT calculations presented in this paper, along with comprehensive comparisons to forthcoming experimental measurements at RHIC and the LHC, pave the way for a novel approach to investigate the α-clustering structure of ^{16}O nuclei using O + O collisions at the ultra-relativistic energies.

I. INTRODUCTION

High-energy heavy ion collisions create an extremely dense and hot environment in which the quarks and gluons confined inside nuclei can be released into a deconfined state of matter known as the quark-gluon plasma (QGP), the hot and dense matter that existed in the early universe. Extensive experimental measurements from the Relativistic Heavy Ion Collider (RHIC) and the Large Hadron Collider (LHC) show the recreation of QGP in the early stage of relativistic nuclear collisions. A crucial experimental evidence of QGP is anisotropic flow. This reflects the hydrodynamical evolution of the QGP, which can transfer the asymmetries in the initial coordinate (geometry) space into anisotropic expansion in the final momentum space [1–3]. The measured different harmonics of the anisotropic flow of the final particles in A + A collisions can be successfully reproduced by hydrodynamic models [4–6], which reveal that QGP behaved nearly perfect fluid. Moreover, recent observations show that anisotropic flow shows similar patterns in small systems such as $p + p$ and p + A [7]. This challenges our current understanding of QGP, as there is controversy over whether hydrodynamics applies to such small systems because of their small size and short lifetime. To study how the system size affects the anisotropic flow of the QGP, collisions of light nuclei at high energies, such as O+O and Ne+Ne collisions, have been proposed [8, 9].

A key aspect of the anisotropic flow is that it provides direct access to the details of the initial conditions of nuclear collisions, thereby exploring the geometric structure of colliding nuclei [10–14]. The nuclear structure of nuclei poses a longstanding challenge and offers an important research opportunity in nuclear physics [15, 16]. Over the years, researchers have continuously attempted to understand the puzzles related to the structure of nuclei using different approaches, especially in the field of low and intermediate-energy nuclear physics [17, 18]. Gamov et al. first proposed that clustered states exist in light nuclei such as ^{12}C, ^{16}O, and ^{20}Ne [19]. Determining the mechanism of the carbon-generated fusion reaction led to the discovery of cluster states [20, 21]. It has been proposed that α-clustering configurations can be detected by sequential decay [22, 23], giant dipole resonances [24–26] or photonuclear reactions [27–30]. In recent years, many studies have revealed the significant role of nuclear structures, such as neutron skin [31, 32] or deformation nuclei [33–35], on some observables in high-energy nuclear collisions. Thus, traditional topics related to nuclear structure can be investigated from a new and unique perspective with high-energy nuclear collisions. The anisotropic flow in high-energy nuclear collisions also serves as an important probe to reveal the geometrical structure of cluster nuclei, which has received significant attention [36–43]. On the other hand, theoretical studies suggest that the 0_6^+ state of ^{16}O is a strong candidate for the 4-α condensed state [44–49]. The condensed α particles are weakly bound in 0S orbits as quasi-bosons, leading to a diffuse and gaseous spatial distribution [50, 51]. Therefore, studying α-clustering structure in O + O collisions at high energies is crucial for understanding many important questions related to nuclear structure, new states of matter, and nuclear astrophysics. Recent theoretical studies also indicate the potential of using high-energy O + O collisions to study the existence of cluster structures within the nuclei of ^{16}O [52–61]. From the experimental side, preliminary results from the STAR ex-

* glma@fudan.edu.cn
† you.zhou@cern.ch

periment demonstrate that anisotropic flow and flow fluctuations can be a powerful tool to study nucleon-nucleon correlations [62–64] in O + O collisions at $\sqrt{s_{\rm NN}} = 200$ GeV [9]. Such efforts will be further strengthened after the operation of O + O collisions at 6.37 TeV at the LHC Run 3 program in 2025 [65].

Various theoretical models, such as thermal, transport, and hydrodynamic models, are used to simulate and study the phase-space evolution of QGP in high-energy heavy ion collisions. Comparison of these model calculations with experimental measurements extracts important information about QGP properties. The transport models describe the dynamic evolution of matter in equilibrium or non-equilibrium states at a more microscopic level and reasonably describe systems with a sufficiently high average number of collisions per particle. A multi-phase transport (AMPT) model successfully describes experimental measurements of anisotropic flow coefficients in large and small systems [66, 67]. Recent studies show that the transport model transforms asymmetries in the initial geometry space into anisotropies in the final momentum space through the parton escape mechanism [68–70], in which the fraction of anisotropic flow increases from small to large systems. By introducing the structure of the initial colliding nuclei into the AMPT model, anisotropic flow in high-energy heavy ion collisions serves as a new probe for exploring the cluster structure of nuclei [38–41, 71]. We are motivated to study the effects of nuclear cluster structure in O + O collisions using the AMPT model. Note that in this work, we utilize the latest improved AMPT model. This model gives better descriptions of more experimental results, especially for centrality dependence of the mean transverse momentum that cannot be reproduced using the public version of the AMPT model.

The paper is organized as follows. First, in Sec. II, we introduce four different geometry configurations of oxygen into the improved AMPT model. In Sec. III, the two-particle correlation method with non-flow subtraction is introduced. In Sec. IV, we present our results on the anisotropic flow and its related observables and compare them with the STAR data in O + O collisions at 200 GeV. Finally, we conclude Sec. V.

II. GEOMETRY CONFIGURATIONS AND AMPT MODEL

Based on the experimental root-mean-square (rms) nuclear charge radius $\left\langle r^2 \right\rangle^{1/2} = 2.6991$ fm for ^{16}O [72], we chose suitable parameters for the four nuclear structures of ^{16}O as follows:

(a) For the Woods-Saxon (W-S) distribution as shown in Fig. 1(a), i.e. the three-parameter Fermi (3pF) model [73] is used for charged density of ^{16}O

$$\rho(r) = \rho_0(1 + wr^2/R_0^2)/(1 + \exp(\frac{r - R_0}{a})), \tag{1}$$

where ρ_0 is the nuclear saturation density, $R_0 = 2.608$ fm is the radius of the nucleus, $a = 0.513$ is the surface diffusion parameter, and $w = -0.051$ is the weight parameter of the 3pF model.

(b) For the tetrahedron-shaped [74–78] and square-shaped cluster structures, the nucleons are arranged as shown in Fig. 1(b) and Fig. 1(c), respectively. The distance between the centers of the clusters is l. The nucleons for each cluster are randomly distributed by the following Gaussian probability distribution,

$$f_i(\mathbf{r}) = \text{const}\ \exp(-\frac{3}{2}\frac{(\mathbf{r} - \mathbf{c_i})^{\mathbf{2}}}{r_c^2}), \tag{2}$$

where $\mathbf{r}$ is the coordinate of the nucleon, $\mathbf{c_i}$ is the center position of cluster i, and r_c is the width of the cluster, i.e., the rms radius of the cluster. For the tetrahedron configuration of the cluster structure, $l = 3.5$ fm and $r_c = 1.23$ fm.

(c) For the square configuration [74, 79] of the cluster structure, $l = 3.0$ fm, $r_c = 1.23$ fm.

(d) For the *ab initio* case of cluster structure, the nucleon density distribution for ^{16}O is obtained by an *ab initio* method based on Nuclear Lattice Effective Field Theory (NLEFT); please see the details in Refs. [56, 61].

Figure 2 presents the nucleon density distributions for the four nuclear structure configurations mentioned above. It can be observed that the nucleon density distributions for the W-S and *ab initio* configurations are significantly higher than that of the tetrahedron and square configurations at the nucleus center. This feature can be inferred from Fig. 1. For the W-S configuration, the nucleons are concentrated more toward the center of the nucleus, while for the tetrahedron and square configurations, there are fewer nucleons at the center of the nucleus.

Next, the above four configurations of ^{16}O are introduced into the initial conditions of the string-melting version of the AMPT (AMPT-SM) model [80] that could describe the evolution of the QGP and the hadrons in high-energy nuclear collisions. This model includes the initial conditions based on the HIJING model, parton interactions in the ZPC model, hadronization with quark-coalescence, and hadron interactions with the ART model. In the AMPT-SM model, the partons are generated by string melting after a formation time of $\tau_0 = E/m_{\rm T}^2$ where E and $m_{\rm T}$ represent the energy and transverse mass of the parent hadron. The positions of the partons are determined based on the positions of their parent hadrons using straight-line trajectories. In this work, we choose a longer effective parton formation time of $\tau_0^{'} = 6.0\tau_0$ to mimic the diffuse density spatial distribution of clustered ^{16}O. The factor of 6.0 was chosen by fitting the STAR measurements on the elliptic flow in O + O collisions at 200 GeV, which will be discussed later. Unlike any publicly available AMPT-SM models, including all the previous AMPT studies on the nuclear structure [12, 53, 58, 81], here we use the latest improved

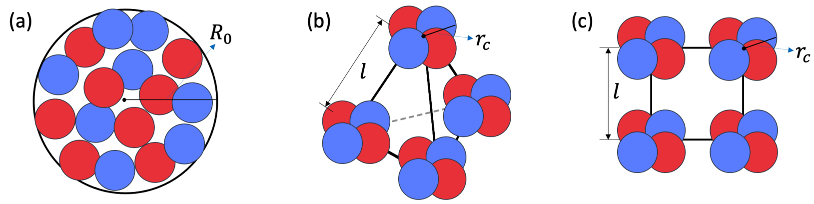

FIG. 1: Illustration of the geometrical configurations of ^{16}O with the nucleon structures of (a) W-S distribution, (b) tetrahedron distribution, and (c) square distribution.

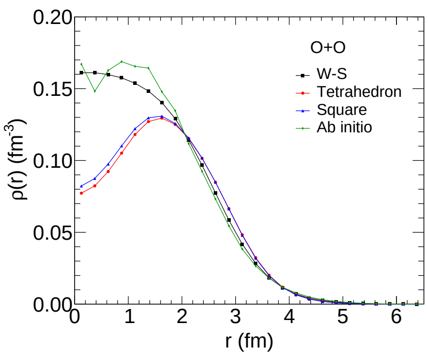

FIG. 2: The nucleon density distributions inside ^{16}O in O+O collisions with the geometrical configurations of W-S, tetrahedron, square, and *ab initio* distributions.

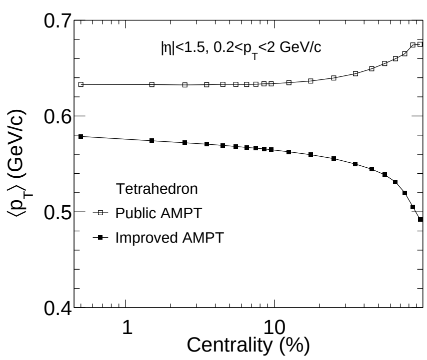

FIG. 3: The centrality dependence of $\langle p_T \rangle$ in O + O collisions at 200 GeV with the tetrahedron configuration of nuclear structure for two versions of AMPT model.

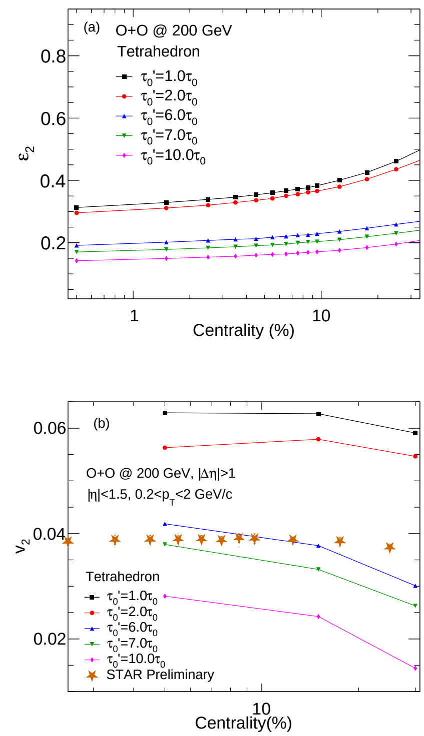

FIG. 4: The centrality dependence of (a) ε_2 and (b) v_2 in O + O collisions at 200 GeV with at different effective parton formation times for the nuclear structure of tetrahedron configuration.

AMPT-SM model with parton cross-section 1.5 mb [82–86]. This improved AMPT-SM model has implemented a new quark coalescence, introduced modern parton distribution functions of the free proton, imparted parameter-dependent nuclear shadowing, and improved heavy flavor productions. The improved model can provide more reasonable descriptions of the particle yield ratios, p_T spectra, and anisotropic flow in A + A collisions at RHIC and LHC energies. It is well-established that the average transverse momentum $\langle p_T \rangle$ is highly sensitive to the initial energy density distribution in collision systems, with $\langle p_T \rangle$ being directly proportional to the temperature T of the system. The $\langle p_T \rangle$ is expected to decrease from central to peripheral collisions, given that central collisions typically exhibit higher temperatures than peripheral ones. As shown in Figure 3, the public AMPT-SM model erroneously predicts an increase in $\langle p_T \rangle$ from central to peripheral collisions in O + O collisions at 200 GeV, which is contrary to the expected trend. In contrast, the improved AMPT-SM model exhibits a more accurate centrality dependence, thanks to the recent incorporation of local nuclear scaling in the initial condition parameters [84]. In this work, we will apply the improved AMPT-SM model for the first time to investigate nuclear structure in high-energy nuclear collisions.

The initial state anisotropy, such as eccentricity ε_2 and triangularity ε_3, characterizes the initial state of nuclear collisions through the event-by-event distribution of the

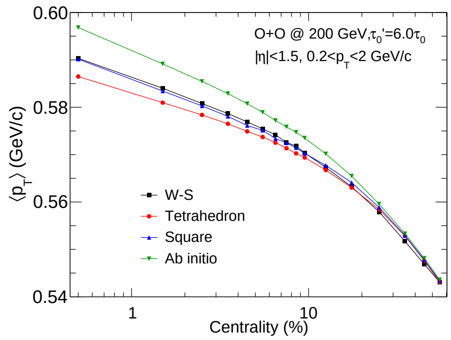

FIG. 5: The centrality dependence of $\langle p_{\mathrm{T}} \rangle$ in $\mathrm{O+O}$ collisions at 200 GeV with different nuclear structure configurations.

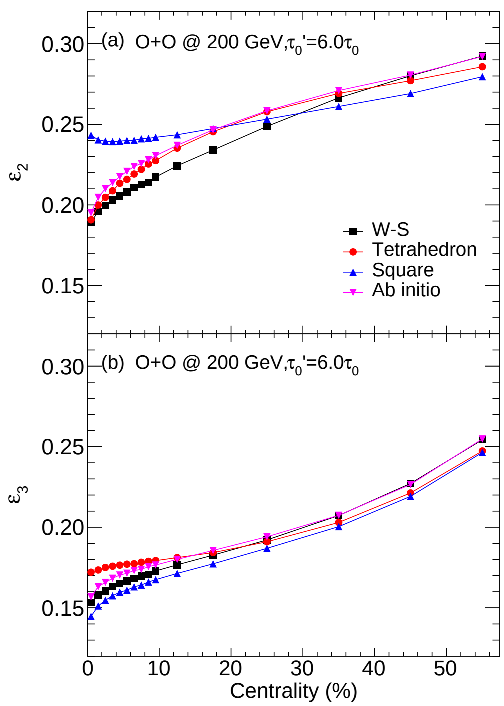

FIG. 6: The centrality dependence of (a) ε_2 and (b) ε_3 in $\mathrm{O+O}$ collisions at 200 GeV with different nuclear structure configurations.

participating partons, which is essential for understanding the initial state geometry [87, 88]. Figure 4 (a) shows the centrality dependence of ε_2 for different effective formation times of $\tau_0^{'} = \tau_0 \sim 10\tau_0$. We find that $\tau_0^{'}$ has a significant effect on ε_2, so ε_2 decreases with increasing $\tau_0^{'}$. Since the linear response of $v_2 \propto \varepsilon_2$ is expected, we present the centrality dependence of v_2 for $\tau_0^{'} = \tau_0 \sim 10\tau_0$ in Fig. 4 (b). We can see that v_2 decreases with $\tau_0^{'}$, since ε_2 decreases with increasing $\tau_0^{'}$. Based on the fact that the v_2 result for $\tau_0^{'} = 6.0\tau_0$ is the closest to the STAR data, we have chosen a factor of 6.0 in our work. It should be noted that although we show only the case for the nuclear structure of the tetrahedron, we have also examined other nuclear structures and observed similar results.

Additionally, we investigated the impact of parton cross-section on v_2. Our findings indicate that obtaining results similar to those of STAR data is challenging, even with a very small cross-section. As a result, we ultimately selected $\tau_0^{'} = 6.0\tau_0$ for further study.

There is a possible reason for the origin of this factor of 6.0. The ground state of ^{16}O has been predicted to be with a tetrahedron structure of 4-α clusters, which is supported by theoretical calculations from the chiral nuclear effective field theory [77], the covariant density functional theory [75], and the algebraic model [78]. On the other hand, with the help of the electromagnetic fields generated in high-energy nuclear collisions (~ 1 MeV per nucleon in $\mathrm{O+O}$ collisions at 200 GeV [89]), the ground state of ^{16}O is likely to excite into its excited 0^+ states which are believed to be with a large occupation probability of 4-α condensate in the $0S$ state [50, 51]. Because the clustered ^{16}O is near the threshold energy and a large fraction of the total binding energy is consumed in forming the α clusters, the condensed α clusters are weakly coupled to each other. This weak coupling results in a dilute and spatially extended density distribution of the clustered ^{16}O [90–92]. We notice that the similar effects of so-called compactness have also been studied in $\mathrm{O+O}$ collisions at 6.5 TeV, using iEBE-VISHNU hydrodynamic simulation with different initial state α-clustering configurations [60]. We expect that measuring the HBT radius is a good way to verify the presence of the diffuse spatial distributions in clustered ^{16}O [93]. A related study is currently in progress.

III. OBSERVABLES AND METHODOLOGY

In this paper, the study of anisotropic flow in $\mathrm{O+O}$ collisions is performed using the two-particle correlation method. By Fourier expansion of the two-particle correlations as

$$\frac{dN^{\mathrm{pairs}}}{d\Delta\phi} \propto 1 + 2\sum_{n=1}^{\infty} v_n \cos(n\Delta\phi), \tag{3}$$

the anisotropic flow can be extracted. Here the relative azimuthal angel of the trigger particle ϕ^{trig} and the associate particle ϕ^{assoc} is $\Delta\phi = \phi^{\mathrm{trig}} - \phi^{\mathrm{assoc}}$. And v_n is the coefficient of the nth-order flow. In order to obtain $v_n(p_{\mathrm{T}}^{\mathrm{trig}})$, the Fourier fitting can be employed on the $Y(\Delta\phi)$ distributions:

$$Y(\Delta\phi, p_{\mathrm{T}}^{\mathrm{trig}}) = c_0(1 + 2\sum_{n=1}^{n=4} c_n \cos(n\Delta\phi)). \tag{4}$$

Then, the non-flow contaminations can be subtracted following

$$c_n^{\mathrm{sub}} = c_n - c_n^{\mathrm{non-flow}} = c_n^{\mathrm{cent}} - c_n^{\mathrm{peri}} \times f, \tag{5}$$

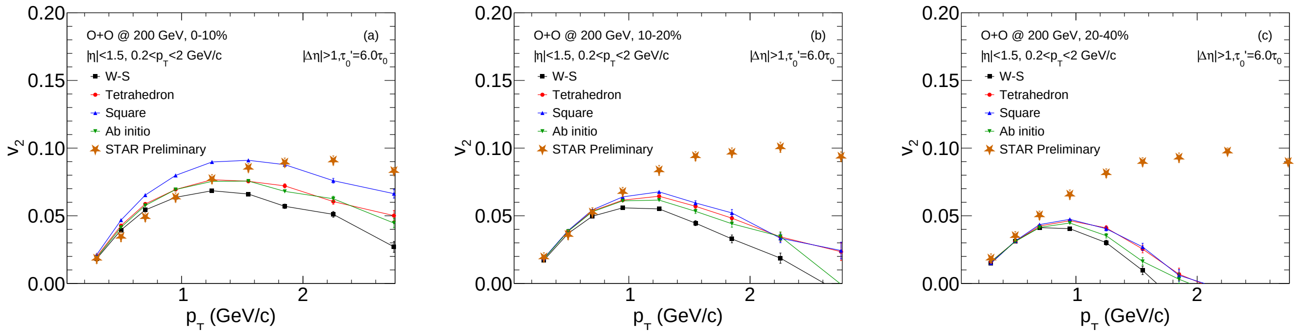

FIG. 7: The p_{T} dependence of v_2 for (a) $0-10\%$, (b) $10-20\%$, and (c) $20-40\%$ centrality bins in $\mathrm{O+O}$ collisions at 200 GeV with different nuclear structure configurations, compared to STAR data.

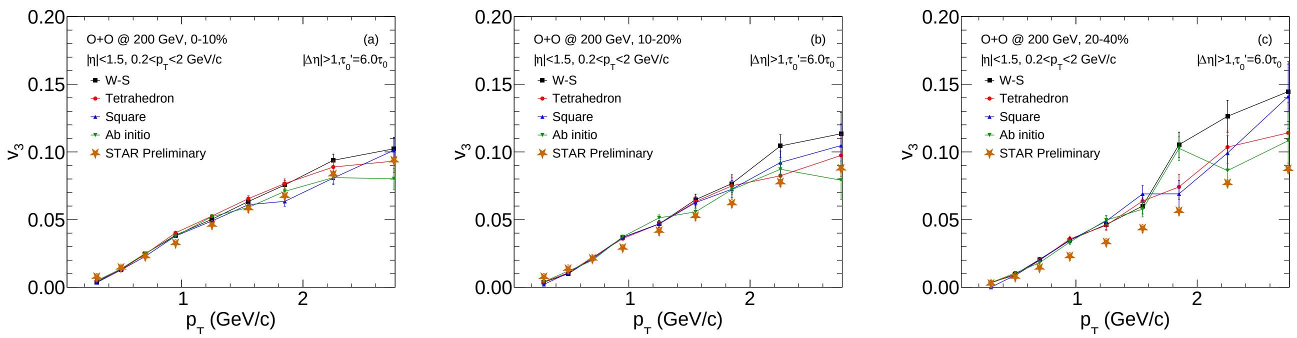

FIG. 8: The p_{T} dependence of v_3 for (a) $0-10\%$, (b) $10-20\%$, and (c) $20-40\%$ centrality bins in $\mathrm{O+O}$ collisions at 200 GeV with different nuclear structure configurations, compared to STAR data.

where $f = c_1^{\mathrm{cent}}/c_1^{\mathrm{peri}}$, c_n is the product of v_n for the trigger and associate particles, i.e. $c_n = v_n^{\mathrm{trig}} \times v_n^{\mathrm{assoc}}$. In this work, the anisotropic flow is extracted using the Fourier fitting and the non-flow subtraction with $60-80\%$ peripheral collisions, as the STAR experiment did [9].

IV. RESULTS AND DISCUSSIONS

Figure 5 shows the centrality dependence of $\langle p_{\mathrm{T}}\rangle$ in $\mathrm{O+O}$ collisions at 200 GeV using $^{16}\mathrm{O}$ structure from the W-S, tetrahedron, square and *ab initio* configurations. The differences in $\langle p_{\mathrm{T}}\rangle$ between the different configurations are very striking, especially for *ab initio* and tetrahedron. For central and mid-central collisions, the $\langle p_{\mathrm{T}}\rangle$ from *ab initio* is higher than the other configurations, while the $\langle p_{\mathrm{T}}\rangle$ from tetrahedral configuration is the smallest. The $\langle p_{\mathrm{T}}\rangle$ of the W-S and square configurations are similar. Meanwhile, compared with Fig. 3, $\langle p_{\mathrm{T}}\rangle$ of tetrahedron for $\tau_0^{'} = 6.0\tau_0$ is very close to $\tau_0^{'} = 1.0\tau_0$. Given the considerable sensitivity of $\langle p_{\mathrm{T}}\rangle$ to v_2, it is reasonable to expect a similar sensitivity of v_2 to different geometric configurations.

Figure 6 (a) and (b) present the AMPT-SM results on the centrality dependence of ε_2 and ε_3 in $\mathrm{O+O}$ collisions at 200 GeV for the W-S, tetrahedron, square, and *ab initio* configurations. We find that both ε_2 and ε_3 increase from central to peripheral collisions. In addition, Fig. 6(a) shows that ε_2 is the largest for the square configuration and the smallest for the W-S configuration in central and mid-central collisions. Meanwhile, Fig. 6(b) shows that the ε_3 is the largest for the tetrahedron configuration and the smallest for the square configuration at central and mid-central collisions. Thus, the simultaneous studies on v_2 and v_3 could provide independent constraints on the nuclear structure.

Transverse momentum-dependent anisotropic flow, $v_n(p_{\mathrm{T}})$, has been a popular tool in ultra-relativistic nuclear collisions. By measuring $v_n(p_{\mathrm{T}})$ of charged and identified particles, one can extract unique information on the initial state geometry and fluctuations, the transport coefficients, the equation of state, and the hadronization mechanism of the QGP. Considering its sensitivity to the initial geometry, it is an ideal probe of nuclear structure in $\mathrm{O+O}$ collisions. Figures 7 (a)-(c) show the p_{T} dependence of v_2 for (a) $0-10\%$, (b) $10-20\%$, and (c) $20-40\%$ centrality bins in $\mathrm{O+O}$ collisions at 200 GeV from the AMPT-SM model, respectively. The calculations from the W-S, tetrahedron, square, and *ab initio* configurations, together with the comparisons to the STAR measurements [9], are presented. We can see that $v_2(p_{\mathrm{T}})$ calculations first increase and then decrease with p_{T} for all the three centrality bins for all configurations of the AMPT-SM model.

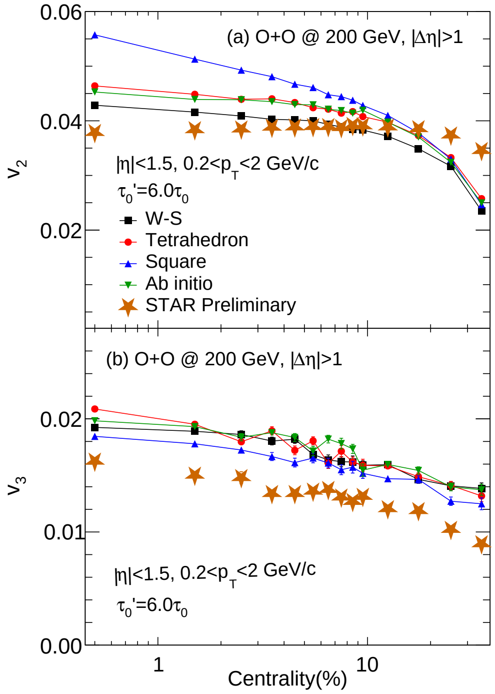

FIG. 9: The centrality dependence of (a) v_2 and (b) v_3 in O + O collisions at 200 GeV with different nuclear structure configurations, compared to STAR data.

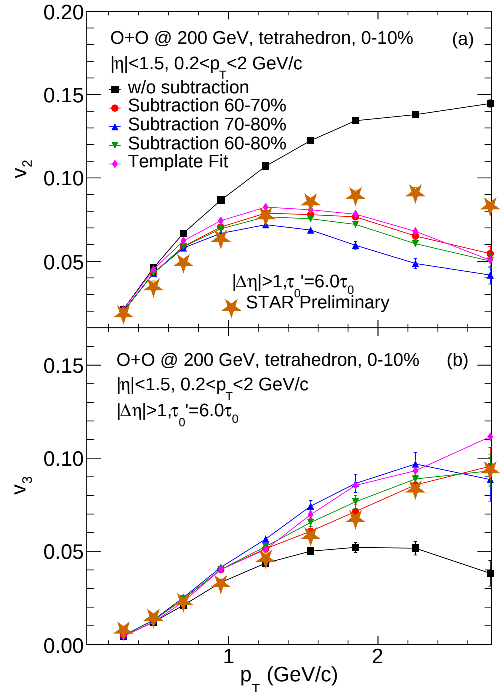

FIG. 11: The p_{T} dependence of (a) v_2 and (b) v_3 for $0-10\%$ centrality bins with different non-flow subtractions in O + O collisions at 200 GeV with tetrahedron configuration, compared to STAR data.

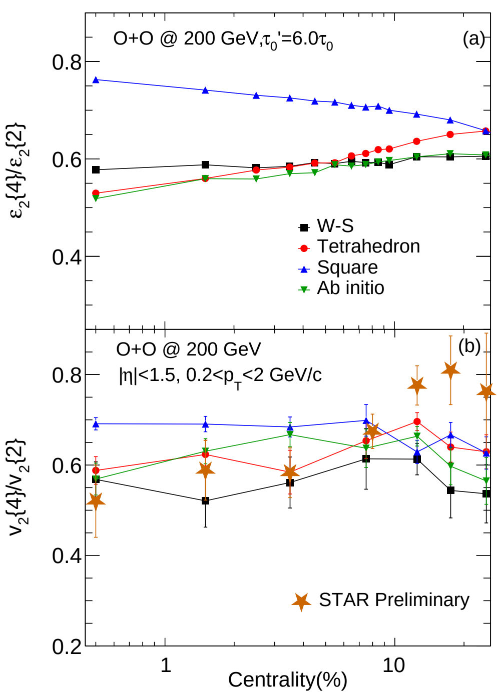

FIG. 10: The centrality dependence of (a) $\varepsilon_2\{4\}/\varepsilon_2\{2\}$ and (b) $v_2\{4\}/v_2\{2\}$ in O + O collisions at 200 GeV with different nuclear structure configurations, compared to STAR data.

Our AMPT-SM calculations can describe STAR measurements for p_{T} below 1 GeV/c but underestimate the experimental data for $p_{\mathrm{T}} > 1$ GeV/c. We also observe the apparent difference among the AMPT-SM results from the different configurations of nuclear structure in $0-10\%$ central collisions. The square configuration shows the largest $v_2(p_{\mathrm{T}})$, whereas the W-S configuration shows the smallest $v_2(p_{\mathrm{T}})$. This can be understood because the square configuration results in a maximum of ε_2 in the transverse plane while the W-S configuration results in a minimum of ε_2 in the central collisions, as shown in Fig. 6 (a).

Similarly, the p_{T} dependence of v_3 for (a) $0-10\%$, (b) $10-20\%$, and (c) $20-40\%$ centrality intervals in O + O collisions at 200 GeV from the AMPT-SM model with different configurations are shown in Fig. 8. It can be seen that v_3 increases linearly as p_{T} increases. The p_{T}-dependent v_3 results from the AMPT-SM model with different configurations show modest differences within the sizable uncertainties, with the result from tetrahedron the largest and the one from square configuration the smallest. All these calculations are compatible with the STAR measurements, and the calculations work particularly well in central collisions.

Figures 9(a) and (b) present the centrality dependence of v_2 and v_3 in O + O collisions at 200 GeV from the AMPT-SM model. Results from the W-S, tetrahedron, square, and *ab initio* configurations are shown, together with the comparisons to the recent STAR measurements [9]. In Fig. 9 (a), the v_2 results from the AMPT-SM model are close to the v_2 measurement from STAR, while the AMPT-SM results present stronger centrality dependence, especially for square configuration. When comparing the AMPT-SM calculations from the four configurations, we find that the difference in v_2 is most pronounced in central collisions, where the square configuration shows the largest v_2 and the W-S configuration shows the smallest v_2, which is consistent with the $p_{\rm T}$-dependent v_2 results in Fig. 7. In Fig. 9 (b), the v_3 results from the AMPT-SM model overestimate the STAR data. The v_3 result for tetrahedron configuration is the largest among all configurations, which is also consistent with the $p_{\rm T}$-dependent v_3 results in Fig. 8. Considering that the $v_3(p_{\rm T})$ result in Fig. 8 is in good agreement with the STAR measurement, it indicates that the $p_{\rm T}$ distributions from the AMPT-SM model may be different from those in actual data. However, since no experimental measurements of the $p_{\rm T}$ distribution are available, we leave a better tuning for future works.

Considering the linear response of the final state anisotropic flow to the initial state geometry, i.e., $v_n \propto \varepsilon_n$ (for the $n = 2, 3$), the study of the anisotropic flow and its event-by-event fluctuations can provide direct access into the initial geometry and its fluctuations. It has been reported recently that the sensitivity to the initial geometry reveals additional information on the structure of the nuclei in the ultra-relativistic nuclear collisions [14, 35, 94]. In this work, we will probe the nuclear structure via the study of the relative flow fluctuation $v_2\{4\}/v_2\{2\}$ and the initial eccentricity fluctuation carried by $\varepsilon_2\{4\}/\varepsilon_2\{2\}$. Here the two- and four-particle cumulant of ε_2 are defined as

$$\varepsilon_2\{2\}^2 \ = \ \left\langle\varepsilon_2^2\right\rangle = \langle\varepsilon_2\rangle^2 + \sigma_{\varepsilon_2}^2, \tag{6}$$

$$\varepsilon_2\{4\}^2 \ = \ (-\left\langle\varepsilon_2^4\right\rangle + 2\left\langle\varepsilon_2^2\right\rangle^2)^{1/2} \approx \langle\varepsilon_2\rangle^2 - \sigma_{\varepsilon_2}^2. \tag{7}$$

where σ_{ε_2} denotes the fluctuations of ε_2. As indicated in Eqs. (6) and (7), a greater σ_{ε_2} leads to a larger deviation of the $\varepsilon_2\{4\}/\varepsilon_2\{2\}$ ratio from unity. The centrality dependence of $\varepsilon_2\{4\}/\varepsilon_2\{2\}$ ratio is shown in Fig. 10(a). We find that for the square configuration, the $\varepsilon_2\{4\}/\varepsilon_2\{2\}$ ratio decreases as centrality increases. Conversely, the $\varepsilon_2\{4\}/\varepsilon_2\{2\}$ ratios for the tetrahedron and *ab initio* configurations exhibit modest increases with centrality, while the results from the W-S configuration show no centrality dependence. Furthermore, the $\varepsilon_2\{4\}/\varepsilon_2\{2\}$ ratio for the square configuration is notably higher than those for the other configurations. This difference among the four configurations is most pronounced in central collisions and diminishes in more peripheral collisions.

Figure 10(b) shows the centrality dependence of $v_2\{4\}/v_2\{2\}$ for the four configurations. Compared to the $\varepsilon_2\{4\}/\varepsilon_2\{2\}$ ratio shown in Fig. 10(a), sizable statistical uncertainties of $v_2\{4\}/v_2\{2\}$ have been seen. Nevertheless, the $v_2\{4\}/v_2\{2\}$ ratio for the square configuration is the largest for the presented centrality ranges, and it decreases with the centrality, whereas for other calculations, the $\varepsilon_2\{4\}/\varepsilon_2\{2\}$ results seem to show an increasing trend toward peripheral collisions. The centrality dependence of $v_2\{4\}/v_2\{2\}$ seem to be consistent with $\varepsilon_2\{4\}/\varepsilon_2\{2\}$ calculations. Furthermore, compared to the STAR measurements on the $v_2\{4\}/v_2\{2\}$ ratio, we found that the results from the tetrahedron and *ab initio* configurations give better descriptions of the STAR measurements than the calculations using W-S and square configurations, despite the sizable uncertainty. Considering the fact that $\langle p_{\rm T}\rangle$ and v_n are sensitive to both the initial conditions as well as the transport properties of QGP, the $v_2\{4\}/v_2\{2\}$ ratio can serve as a better probe of the nuclear structure as it is robust against the system's dynamic evolution. The presented $v_2\{4\}/v_2\{2\}$ results seem to suggest the cluster structure for ^{16}O; they shed new light on using ultra-relativistic nuclear collisions to complement the low-energy nuclear structure studies.

To eventually understand the existing discrepancy between the AMPT flow calculations and STAR measurements, we perform careful investigations on the non-flow effects on the anisotropic flows in this work. Figures 11 (a) shows the $v_2(p_{\rm T})$ with four different non-flow subtractions, including subtraction with $60-70\%$ collisions, subtraction with $70-80\%$ collisions, subtraction with $60-80\%$ collisions, and template fit method, for tetrahedron configuration at $0-10\%$ centrality. The results without nonflow subtraction but directly from the Fourier fit are also presented for comparison. Due to the largest non-flow effect, the $v_2(p_{\rm T})$ without subtraction is the largest, especially at high $p_{\rm T}$. While $v_2(p_{\rm T})$ for non-flow subtractions with $70-80\%$ collisions is the smallest, possibly because non-flow is over-subtracted. The template fit method gives the similar $v_2(p_{\rm T})$ results as non-flow subtractions with $60-70\%$ collisions. Considering that the peripheral subtraction method treats the entire correlation observed in peripheral collisions as nonflow, it usually serves the lower limit of flow, whereas the template fit takes care of the flow modulation in the peripheral collisions; it usually provides an upper limit of flow. Thus, one would expect the true flow results to be somewhat located between v_2 from the template and peripheral subtraction method, while such a range could not cover the STAR measurement based on the template fit method. Figure 11 (b) shows the $v_3(p_{\rm T})$ with the four different non-flow subtractions and the results without non-flow subtraction. v_2 originates from the initial geometry of the collision region, while v_3 arises from the fluctuations in the initial geometry and subsequent hydrodynamic evolution. In contrast to $v_2(p_{\rm T})$, the non-flow subtraction approaches have the opposite effect on $v_3(p_{\rm T})$: the $v_3(p_{\rm T})$ without subtraction is the smallest, while $v_3(p_{\rm T})$ for non-flow subtractions with $70-80\%$ collisions is the largest. This is because the fluctuation-induced $v_3(p_{\rm T})$ signal is more pronounced after subtracting the more non-flow contribution. It is also noticed that various non-flow subtraction methods do not yield a significant difference in $v_3(p_{\rm T})$, which is not the case observed in the non-flow study of $v_2(p_T)$. The reasonable agreement of AMPT calculations and STAR measurement in $v_3(p_T)$ persists, independent of what non-flow subtraction method is applied.

V. SUMMARY

To summarize, we utilized the improved AMPT-SM model, which describes more experimental results, to analyze the anisotropic flow and related observables for the W-S, tetrahedron, square, and *ab initio* configurations in O + O collisions at 200 GeV. We found that the AMPT-SM model, when adjusted for a longer effective parton formation time $\tau_0^{'} = 6.0\tau_0$, aligns better with the STAR data. Employing the same experimental method of non-flow subtraction, we noted that the p_T-dependent v_2 closely matches the STAR $v_2(p_T)$ measurement at lower p_T values, yet it underestimates the measurements at higher p_T. The p_T-dependent v_3, however, is consistent with the STAR measurements across the entire p_T range. Additionally, the integrated v_2 results are comparable in magnitude to the STAR measurements, while the integrated v_3 values from the AMPT-SM model are marginally higher than the observed v_3. In contrast to typical v_n studies, the $\varepsilon_2\{4\}/\varepsilon_2\{2\}$ ratio demonstrates reduced sensitivity to dynamic evolution and robust sensitivity to fluctuations originating from nuclear structures. Our findings indicate that the implementation of α-clustering structures yields a more accurate description of the STAR $v_2\{4\}/v_2\{2\}$ measurements.

The presented studies, particularly using the latest developments of the AMPT-SM model for the first time, provide insights into the presence of the cluster structures in ^{16}O nuclei. The findings suggest that the anisotropic flow observables can serve as a sensitive probe for diagnosing the different configurations of the ^{16}O structure in high-energy nuclear collisions. This opens up new possibilities for studying the nuclear structure and exploring the cluster structure of nuclei using high-energy O + O collisions. Future studies can build upon these findings and further investigate the nuclear structure in the O+O collisions using more experimental measurements on the anisotropic flow phenomena at RHIC and the ongoing LHC Run 3 program.

Acknowledgments

We thank Prof. Bo Zhou and Dr. Chun-Jian Zhang for helpful discussions about cluster structure for ^{16}O and anisotropic flow for O + O collisions. In addition, we gratefully acknowledge Prof. Dean Lee and Prof. Christopher Plumberg for sharing the nucleon density distribution of oxygen nuclei. Finally, we acknowledge Dr. Chen Zhong for maintaining the high-quality performance of the Fudan supercomputing platform for nuclear physics. This work is supported by the National Natural Science Foundation of China under Grant No. 12105054 (X.Z.), the European Union (ERC, InitialConditions), the VILLUM FONDEN (grant number 00025462), and Independent Research Fund Denmark (Y.Z.), the National Natural Science Foundation of China under Grants No.12325507, No.12147101, No. 11961131011, No. 11890710, No. 11890714, No. 11835002, the Strategic Priority Research Program of Chinese Academy of Sciences under Grant No. XDB34030000, and the Guangdong Major Project of Basic and Applied Basic Research under Grant No. 2020B0301030008 (G.M.), the National Science Foundation under Grant No. 2310021 (Z.W.L.).

[1] J.-Y. Ollitrault, Phys. Rev. D **46**, 229 (1992).
[2] U. Heinz and R. Snellings, Ann. Rev. Nucl. Part. Sci. **63**, 123 (2013), 1301.2826.
[3] W. Zhao, Y. Zhou, H. Xu, W. Deng, and H. Song, Phys. Lett. B **780**, 495 (2018), 1801.00271.
[4] J. Adams et al. (STAR), Nucl. Phys. A **757**, 102 (2005), nucl-ex/0501009.
[5] H. Song, Y. Zhou, and K. Gajdosova, Nucl. Sci. Tech. **28**, 99 (2017), 1703.00670.
[6] T. Hirano, N. van der Kolk, and A. Bilandzic, Lect. Notes Phys. **785**, 139 (2010), 0808.2684.
[7] S. Acharya et al. (ALICE), Phys. Rev. Lett. **123**, 142301 (2019), 1903.01790.
[8] J. Brewer, A. Mazeliauskas, and W. van der Schee, in *Opportunities of OO and pO collisions at the LHC* (2021), 2103.01939.
[9] S. Huang (2023), 2312.12167.
[10] S. Acharya et al. (ALICE), Phys. Lett. B **784**, 82 (2018), 1805.01832.
[11] S. Acharya et al. (ALICE), Phys. Lett. B **834**, 137393 (2022), 2111.06106.
[12] C. Zhang and J. Jia, Phys. Rev. Lett. **128**, 022301 (2022), 2109.01631.
[13] C. Zhang, S. Bhatta, and J. Jia, Phys. Rev. C **106**, L031901 (2022), 2206.01943.
[14] Z. Lu, M. Zhao, X. Li, J. Jia, and Y. Zhou, Eur. Phys. J. A **59**, 279 (2023), 2309.09663.
[15] Y.-G. Ma, Nuclear Techniques **46**, 08001 (2023).
[16] Y. Liu and Y.-L. Ye, Nucl. Sci. Tech. **29**, 184 (2018).
[17] D.-Q. Fang, Nuclear Techniques **46**, 080016 (2023).
[18] C.-W. Ma, Y.-P. Liu, H. Wei, J. Pu, K. Cheng, and Y.-T. Wang, Nucl. Sci. Tech. **33**, 6 (2022), 2201.01442.
[19] G. Gamow, Lond. Proc. Ser. A **126**, 632 (1930).
[20] F. Hoyle, Astrophys. J. Suppl. **1**, 121 (1954).
[21] C. W. Cook, W. A. Fowler, C. C. Lauritsen, and T. Lauritsen, Phys. Rev. **107**, 508 (1957).
[22] J. Bishop et al., Phys. Rev. C **100**, 034320 (2019), 1907.05471.
[23] Z. H. Yang et al., Phys. Rev. Lett. **131**, 242501 (2023).
[24] W. B. He, Y. G. Ma, X. G. Cao, X. Z. Cai, and G. Q. Zhang, Phys. Rev. Lett. **113**, 032506 (2014), 1407.5414.
[25] W. B. He, Y. G. Ma, X. G. Cao, X. Z. Cai, and G. Q.

Zhang, Phys. Rev. C **94**, 014301 (2016), 1602.08955.
[26] S. S. Wang, Y. G. Ma, W. B. He, D. Q. Fang, and X. G. Cao, Phys. Rev. C **108**, 014609 (2023).
[27] B. S. Huang, Y. G. Ma, and W. B. He, Phys. Rev. C **95**, 034606 (2017), 1803.07972.
[28] B.-S. Huang, Y.-G. Ma, and W.-B. He, Eur. Phys. J. A **53**, 119 (2017).
[29] B.-S. Huang and Y.-G. Ma, Phys. Rev. C **101**, 034615 (2020), 2006.00722.
[30] C.-Z. Shi and Y.-G. Ma, Nucl. Sci. Tech. **32**, 66 (2021), 2109.09938.
[31] H. Li, H.-j. Xu, Y. Zhou, X. Wang, J. Zhao, L.-W. Chen, and F. Wang, Phys. Rev. Lett. **125**, 222301 (2020), 1910.06170.
[32] G. Giacalone, G. Nijs, and W. van der Schee, Phys. Rev. Lett. **131**, 202302 (2023), 2305.00015.
[33] B. Bally, M. Bender, G. Giacalone, and V. Somà, Phys. Rev. Lett. **128**, 082301 (2022), 2108.09578.
[34] W. Ryssens, G. Giacalone, B. Schenke, and C. Shen, Phys. Rev. Lett. **130**, 212302 (2023), 2302.13617.
[35] E. G. D. Nielsen, F. K. Rømer, K. Gulbrandsen, and Y. Zhou, Eur. Phys. J. A **60**, 38 (2024), 2312.00492.
[36] W. Broniowski and E. Ruiz Arriola, Phys. Rev. Lett. **112**, 112501 (2014), 1312.0289.
[37] P. Bozek, W. Broniowski, E. Ruiz Arriola, and M. Rybczynski, Phys. Rev. C **90**, 064902 (2014), 1410.7434.
[38] S. Zhang, Y. G. Ma, J. H. Chen, W. B. He, and C. Zhong, Phys. Rev. C **95**, 064904 (2017), 1702.02507.
[39] S. Zhang, Y. G. Ma, J. H. Chen, W. B. He, and C. Zhong, Eur. Phys. J. A **54**, 161 (2018), 1808.10265.
[40] J. He, W.-B. He, Y.-G. Ma, and S. Zhang, Phys. Rev. C **104**, 044902 (2021), 2109.06277.
[41] Y.-G. Ma and S. Zhang, pp. 1–30 (2022), 2206.08218.
[42] P. Dasgupta, G.-L. Ma, R. Chatterjee, L. Yan, S. Zhang, and Y.-G. Ma, Eur. Phys. J. A **57**, 134 (2021), 2007.09543.
[43] P. Dasgupta, R. Chatterjee, and G.-L. Ma, Phys. Rev. C **107**, 044908 (2023), 2204.00235.
[44] Y. Funaki, T. Yamada, H. Horiuchi, G. Ropke, P. Schuck, and A. Tohsaki, Phys. Rev. Lett. **101**, 082502 (2008), 0802.3246.
[45] S. Ohkubo (2013), 1301.7485.
[46] T. Suhara, Y. Funaki, B. Zhou, H. Horiuchi, and A. Tohsaki, Phys. Rev. Lett. **112**, 062501 (2014), 1310.7684.
[47] Y. Funaki, T. Yamada, H. Horiuchi, G. RöPke, P. Schuck, and A. Tohsaki, Few Body Syst. **54**, 521 (2013).
[48] Y. Funaki, T. Yamada, H. Horiuchi, G. Ropke, P. Schuck, and A. Tohsaki, Mod. Phys. Lett. A **25**, 1939 (2010).
[49] Y. Funaki, T. Yamada, H. Horiuchi, G. Ropke, P. Schuck, and A. Tohsaki, Int. J. Mod. Phys. A **24**, 1995 (2009).
[50] Y. Funaki, H. Horiuchi, W. von Oertzen, G. Ropke, P. Schuck, A. Tohsaki, and T. Yamada, Phys. Rev. C **80**, 064326 (2009), 0912.2934.
[51] P. Schuck, Y. Funaki, H. Horiuchi, G. Röpke, A. Tohsaki, and T. Yamada, Phys. Scripta **91**, 123001 (2016), 1702.02191.
[52] M. Rybczyński and W. Broniowski, Phys. Rev. C **100**, 064912 (2019), 1910.09489.
[53] Y.-A. Li, S. Zhang, and Y.-G. Ma, Phys. Rev. C **102**, 054907 (2020), 2010.10003.
[54] Y.-A. Li, D.-F. Wang, S. Zhang, and Y.-G. Ma, Phys. Rev. C **104**, 044906 (2021), 2110.04784.
[55] D. Behera, N. Mallick, S. Tripathy, S. Prasad, A. N. Mishra, and R. Sahoo, Eur. Phys. J. A **58**, 175 (2022), 2110.04016.
[56] N. Summerfield, B.-N. Lu, C. Plumberg, D. Lee, J. Noronha-Hostler, and A. Timmins, Phys. Rev. C **104**, L041901 (2021), 2103.03345.
[57] C. Ding, L.-G. Pang, S. Zhang, and Y.-G. Ma, Chin. Phys. C **47**, 024105 (2023).
[58] D. Behera, S. Prasad, N. Mallick, and R. Sahoo, Phys. Rev. D **108**, 054022 (2023), 2304.10879.
[59] D. Behera, S. Deb, C. R. Singh, and R. Sahoo, Phys. Rev. C **109**, 014902 (2024).
[60] Y. Wang, S. Zhao, B. Cao, H.-j. Xu, and H. Song (2024), 2401.15723.
[61] G. Giacalone et al. (2024), 2402.05995.
[62] A. Gezerlis, I. Tews, E. Epelbaum, S. Gandolfi, K. Hebeler, A. Nogga, and A. Schwenk, Phys. Rev. Lett. **111**, 032501 (2013), 1303.6243.
[63] N. Fomin, D. Higinbotham, M. Sargsian, and P. Solvignon, Ann. Rev. Nucl. Part. Sci. **67**, 129 (2017), 1708.08581.
[64] Z. Ye and J. Arrington, in *13th Conference on the Intersections of Particle and Nuclear Physics* (2018), 1810.03667.
[65] S. Acharya et al. (ALICE) (2021).
[66] A. Bzdak and G.-L. Ma, Phys. Rev. Lett. **113**, 252301 (2014), 1406.2804.
[67] G.-L. Ma and Z.-W. Lin, Phys. Rev. C **93**, 054911 (2016), 1601.08160.
[68] L. He, T. Edmonds, Z.-W. Lin, F. Liu, D. Molnar, and F. Wang, Phys. Lett. B **753**, 506 (2016), 1502.05572.
[69] G.-L. Ma and A. Bzdak, Nucl. Phys. A **956**, 745 (2016).
[70] L. Ma, G.-L. Ma, and Y.-G. Ma, Phys. Rev. C **103**, 014908 (2021), 2102.01872.
[71] Y.-X. Zhang, S. Zhang, and Y.-G. Ma (2024), 2403.04362.
[72] I. Angeli and K. P. Marinova, Atom. Data Nucl. Data Tabl. **99**, 69 (2013).
[73] H. De Vries, C. W. De Jager, and C. De Vries, Atom. Data Nucl. Data Tabl. **36**, 495 (1987).
[74] W. Bauhoff, H. Schultheis, and R. Schultheis, Phys. Rev. C **29**, 1046 (1984).
[75] and, Chinese Physics C **36**, 818 (2012), URL https://dx.doi.org/10.1088/1674-1137/36/9/004.
[76] M. Girod and P. Schuck, Phys. Rev. Lett. **111**, 132503 (2013), 1309.6104.
[77] E. Epelbaum, H. Krebs, T. A. Lähde, D. Lee, U.-G. Meißner, and G. Rupak, Phys. Rev. Lett. **112**, 102501 (2014), 1312.7703.
[78] R. Bijker and F. Iachello, Phys. Rev. Lett. **112**, 152501 (2014), 1403.6773.
[79] D. M. Brink, H. Friedrich, A. Weiguny, and C. W. Wong, Phys. Lett. B **33**, 143 (1970).
[80] Z.-W. Lin, C. M. Ko, B.-A. Li, B. Zhang, and S. Pal, Phys. Rev. C **72**, 064901 (2005), nucl-th/0411110.
[81] J. Jia, G. Giacalone, and C. Zhang, Phys. Rev. Lett. **131**, 022301 (2023), 2206.10449.
[82] C. Zhang, L. Zheng, F. Liu, S. Shi, and Z.-W. Lin, Phys. Rev. C **99**, 064906 (2019), 1903.03292.
[83] L. Zheng, C. Zhang, S. S. Shi, and Z. W. Lin, Phys. Rev. C **101**, 034905 (2020), 1909.07191.
[84] C. Zhang, L. Zheng, S. Shi, and Z.-W. Lin, Phys. Rev. C **104**, 014908 (2021), 2103.10815.
[85] C. Zhang, L. Zheng, S. Shi, and Z.-W. Lin, Phys. Lett. B **846**, 138219 (2023), 2210.07767.

[86] C. Zhang, Z.-W. Lin, L. Zheng, and S. Shi, in *11th International Conference on Hard and Electromagnetic Probes of High-Energy Nuclear Collisions: Hard Probes 2023* (2023), 2309.01215.

[87] B. Alver and G. Roland, Phys. Rev. C **81**, 054905 (2010), [Erratum: Phys.Rev.C 82, 039903 (2010)], 1003.0194.

[88] L. Ma, G. L. Ma, and Y. G. Ma, Phys. Rev. C **94**, 044915 (2016), 1610.04733.

[89] J. Zhao, J.-H. Chen, X.-G. Huang, and Y.-G. Ma, Nucl. Sci. Tech. **35**, 20 (2024), 2211.03968.

[90] S. Ohkubo and Y. Hirabayashi, Phys. Rev. C **75**, 044609 (2007), 1102.1771.

[91] M. Tomita, M. Iwasaki, R. Otani, and M. Ito, Phys. Rev. C **89**, 034619 (2014).

[92] B. Zhou, Y. Funaki, H. Horiuchi, Y.-G. Ma, G. Röpke, P. Schuck, A. Tohsaki, and T. Yamada, Nature Commun. **14**, 8206 (2023).

[93] J. He, S. Zhang, Y.-G. Ma, J. Chen, and C. Zhong, Eur. Phys. J. A **56**, 52 (2020), 2002.06058.

[94] J. Jia, Phys. Rev. C **105**, 044905 (2022), 2109.00604.